PHOTONICS Research

Extremely narrow resonant linewidths in metal-dielectric heterostructures

JIE ZHENG,[1,2] JINFENG ZHU,[3] AND ZHILIN YANG[1,*]

[1]Department of Physics, Collaborative Innovation Center for Optoelectronic Semiconductors and Efficient Devices, Jiujiang Research Institute, Xiamen University, Xiamen 361005, China
[2]Laboratory of Micro-Nano Optics, School of Physics and Electronic Engineering, Sichuan Normal University, Chengdu 610101, China
[3]Department of Electronic Science, Xiamen University, Xiamen 361005, China
*Corresponding author: zlyang@xmu.edu.cn

Received 10 March 2022; revised 5 April 2022; accepted 6 April 2022; posted 7 April 2022 (Doc. ID 458049); published 30 June 2022

Plasmonic high-quality factor resonators with narrow surface plasmon resonance (SPR) linewidths are extremely significant for surface-enhanced Raman scattering, optical sensors, imaging, and color filters. Unfortunately, extensive research on narrowing SPR linewidths is mainly based on noble metal nanostructures that are restricted by intrinsic loss. Here, heterostructures consisting of metal and dielectric metaphotonics are experimentally designed and fabricated for elaborating SPR linewidths. The results demonstrate that the SPR linewidths can be narrowed by 66.7% relative to that of aluminum nanostructures. The resonant linewidths are directly shrunk due to the interaction between low loss in the semiconductor nanostructures and electromagnetic confinement in the metal counterparts. Meanwhile, the resonant wavelength governed by heterostructure configurations shifts from 600 to 930 nm. This work will pave an avenue toward controlling resonant linewidths of metal-dielectric heterostructures for numerous applications.

https://doi.org/10.1364/PRJ.458049

1. INTRODUCTION

Plasmonic nanostructures with delicate surface plasmon resonance (SPR) line shapes have been of particular interest in recent years [1–4]. The linewidths refer to the full-width at half-maximum (FWHM) of the resonant peaks/valleys of the plasmonic nanostructures. The narrow SPR linewidths are advantageous for biochemical sensors, nanolasers, and optical imaging. An efficient way to narrow SPR linewidths is to assemble periodic arrays by utilizing diffractive coupling with neighboring particles [5,6]. Crozier's group demonstrated narrow near-infrared resonance peaks in two-dimensional gold nanoparticle arrays by coupling between grating diffraction and localized surface plasmons [7]. Ren's group achieved the narrowest linewidth of 3 nm at 960 nm in gold hexagonal arrays [8]. Additionally, in the last few years, a host of strategies or efforts have been devoted to achieving narrower linewidths, including reducing the surface roughness [9], designing the patterns of plasmonic nanostructures [10–12], choosing the materials of the metallic layer [13], and forming bound states in the continuum (BIC) of plasmonic-photonic systems [14–16]. However, extensive attention to narrowing SPR linewidths has mainly focused on noble metal nanostructures, which can support SPR from the visible to the THz wavelength regimes [15,17,18]. To achieve narrow SPR linewidths in the UV wavelength band, our group manufactured stable aluminum (Al) plasmonic arrays and achieved a 14-nm narrow SPR linewidth at about a 400-nm wavelength [19]. The unsatisfactory reality of Al nanostructures is the high level of intrinsic ohmic losses [20]. Recently, dielectric nanostructures with high refractive indices have emerged to be a contender in low losses [21,22]. The integration of metallic nanostructures with dielectric nanostructures is demonstrated to mitigate losses [23]. Fortunately, the cooperative interaction between metal and dielectric nanostructures has given rise to vast and novel optical phenomena for functional photonic devices [24–31]. However, it is one of the major issues in narrowing resonant linewidths based on heterostructures. Here, we put forward an efficient strategy to mitigate the losses in plasmonic nanostructures by integrating dielectric nanostructures with Al nanostructures. The motivation for adopting metal-dielectric heterostructures is because the interaction of a lossy Al plasmonic cavity and a lossless dielectric cavity can reduce the non-radiation loss in the near-infrared regime.

In this work, we experimentally design and manufacture a hybrid plasmonic nanostructure consisting of Al and silicon (Si). The Al can support SPR in a wide spectrum from deep ultraviolet (DUV) to near-infrared (NIR) regions. Despite using a Si semiconductor with an indirect bandgap, Si nanostructures are luminescent and can be integrated into a chip. In addition, Si has a large permittivity ($n > 3.5$) and a low imaginary part of the refractive index in the visible and the NIR

spectral ranges (see Appendix A.1). Importantly, Si has a relatively low cost and process compatibility. Therefore, the integrated Al-Si heterostructure enables narrowing SPR linewidths and reduces the non-radiation loss. High refractive index (Si) in the heterostructures can shrink the pronounced SPR linewidths by a factor of about 66.7%. Meanwhile, the resonant wavelength can shift from 600 to 930 nm.

Generally, the heterostructures of metal-dielectric nanostructures are first fabricated individually and then combined by utilizing sophisticated techniques, such as drop casting and molecule linking [32]. In this article, we propose a straightforward fabrication technology for manufacturing heterostructures that are schematically illustrated in Fig. 1(a). Primarily, photoresist nanohole patterns with a 450-nm periodicity and a 250-nm diameter are fabricated on silicon wafers by utilizing nanoimprint lithography (NIL). The fabrication details can be found in Appendix A. Si nanoholes with 100-nm depths are formed via an inductively coupled plasma (ICP) etching system that utilizes photoresist nanoholes as a mask. Finally, a thin Al film 80-nm-thick covers the surface by TEMD-500 thermal evaporation. The residual photoresist layer acts as a spacer, and the thickness is ~2 nm displayed in pink, as shown in Fig. 1(a). Figure 1(b) displays the top-view scanning electron microscopy (SEM) image of heterostructures with a 450-nm period and ~240 nm width of nanoholes. The geometrical parameters of H_1 and H_2, in the inset of Fig. 1(b), denote the Al film thicknesses covering the top and side wall of the Si nanoholes, respectively. The values of H_1 and H_2 are about 80 and 10 nm. Remarkably, due to the deposition of the 80-nm Al film, size variations in the experimentally fabricated heterostructures nanoholes are inevitable. Additionally, Fig. 1(c) shows that the Al/Si elemental ratio of the heterostructures characterized by energy dispersive X-ray spectroscopy (EDX) is 13.14/81.61.

2. RESULTS AND DISCUSSION

The Al can support the surface plasmon resonance (SPR) covering from the DUV to NIR regions and is the best candidate for plasmonics in the UV region. However, Al plasmonic nanostructures are restricted by high losses resulting from the difficulty in narrowing resonant linewidths. Fortunately, dielectric nanostructures with low loss can manipulate light at the nanoscale like plasmonic nanostructures. New energies now focus on integrating high-refractive-index dielectric nanostructures and plasmonic nanostructures into the heterostructures to narrow the SPR linewidths. To verify the superiority of introducing Si nanostructures, therein, the reflectance spectra of the Al-Si heterostructures nanoholes are recorded by utilizing a home-built angle-resolved reflectance spectrometer (see Appendix A.2) with varied illumination angles (θ) and azimuthal angles (φ). Figure 2(a) shows the diagram of the home-built angle-resolved reflectance spectrometer. We investigate the optical response of the heterostructures to varied θ. For simplification, φ is 0°. When θ increases from 0° to 75°, we can obviously observe that the resonant mode emerges red shift and becomes narrower. The characteristic resonant modes of the heterostructures are similar to that of the plasmonic Al nanostructures. Thus, we can quantitatively analyze the resonant modes according to the phase-matching equations [4,19,33],

$$\frac{2\pi}{\lambda_{SPP}}\sqrt{\frac{\varepsilon_{Al}\cdot\varepsilon}{\varepsilon_{Al}+\varepsilon}} = \sqrt{\left(\frac{2\pi}{\lambda_{SPP}}\sin\theta\sin\varphi+m\frac{2\pi}{P}\right)^2+\left(\frac{2\pi}{\lambda_{SPP}}\sin\theta\cos\varphi+n\frac{2\pi}{P}\right)^2}, \tag{1}$$

where λ_{SPP} denotes the surface plasmon polariton (SPP) resonant wavelength, ε_{Al} and ε represent the permittivity of the Al and the dielectric, (m, n) is the order of the SPP resonant modes, and θ, φ, and P are the incidence angle, azimuthal angle, and periodic parameter, respectively. The resonant mode of the heterostructures attributes to the $(-1, 0)$ SPP mode according to Eq. (1) [4]. Figure 2(b) demonstrates that the $(-1, 0)$ SPP resonant mode dominates the optical coupling to the electronic excitations in the Al-Si heterostructures.

Next, we investigate the optical response of the resonant wavelengths and the linewidths of the heterostructures to the varied φ in the case of a constant θ of 75°. The reflectance spectra in full φ range with steps of 5° are shown in Fig. 2(c). We can distinctly observe that the $(-1, 0)$ SPP mode red shifts and blue shifts when the φ is larger than 45°. When the θ equals to 45°, the bandgap of ~50 nm occurs, which originates from the strong interference between the $(-1, 0)$ SPP modes and the hybrid modes of the heterostructures [4,19,33]. In Fig. 2(d), the resonant peak of the heterostructures exhibits a broader shifting from 600 to 930 nm with the increase of the

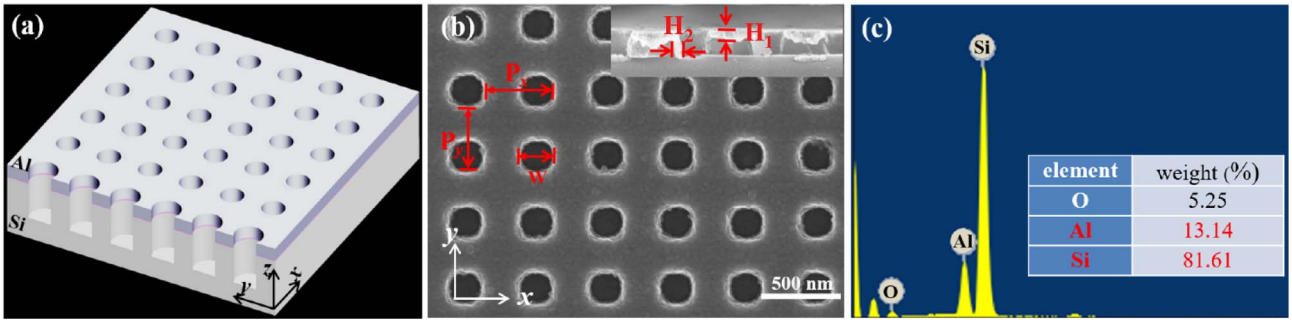

Fig. 1. (a) Schematic illustration of the heterostructures. (b) Top-view SEM image of heterostructures, where P_x equal to P_y denotes the 450 nm period and W the 240 nm width of the nanoholes, H_1 the top thickness of 80 nm, and H_2 the vertical wall thickness of ~10 nm. (c) The element components of Al and Si.

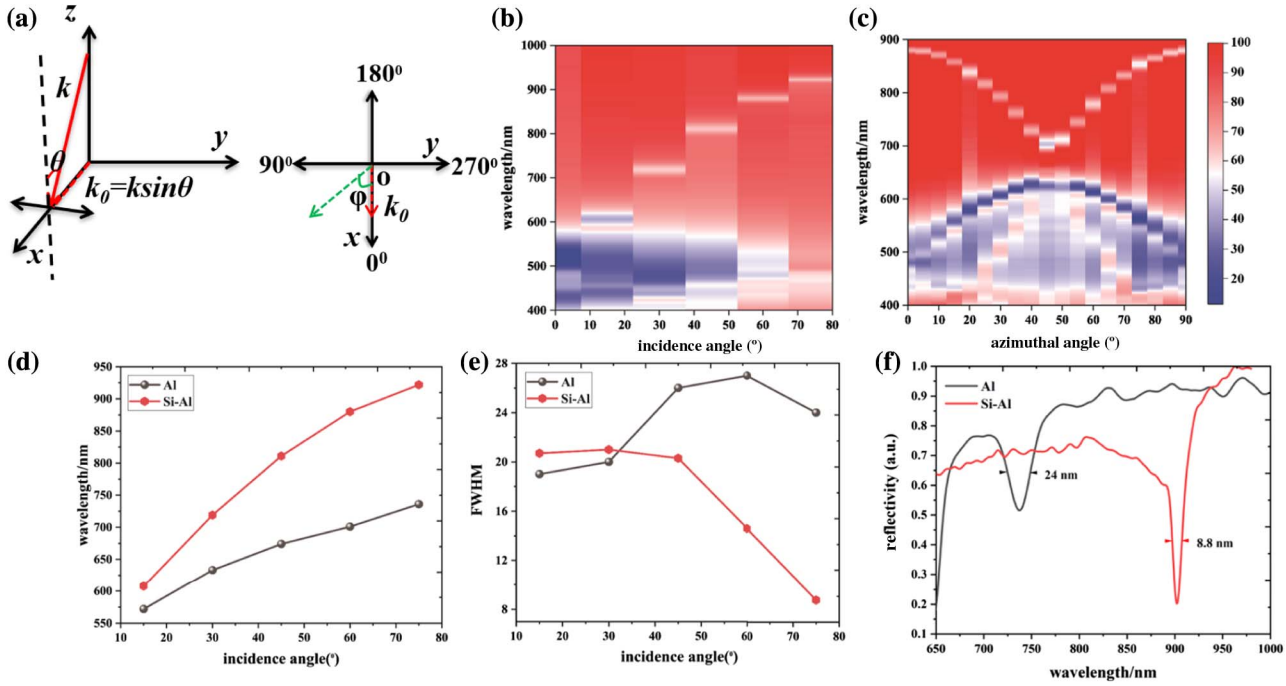

Fig. 2. For the spectral analysis, the reflection spectra under different incidence angles and azimuthal angles were collected by the angle-resolved spectrometer. (a) The diagram of the angle-resolved spectrometer, and θ and φ defined as illumination angle and azimuthal angle, respectively. (b) and (c) The variation of the optical properties with θ and φ, respectively, in case of illumination by an unpolarized white light. (d) The reflectance spectra of the Al nanostructures and the Al-Si heterostructures under varied illumination angle with φ set as 0°. (e) The FWHM of the pure Al nanostructures and the Al-Si heterostructures under the varied illumination angle with φ set as 0°. (f) The resonant linewidth comparison of the pure Al nanostructures and the Al-Si heterostructures under an incidence angle set as 75° with φ set as 0°.

illumination angles. Compared with that of the Al nanostructures, the Al-Si heterostructures display a prominent controllability in a wide wavelength range. In Fig. 2(e), the resonant peak of the Al-Si heterostructures, upon being compared with the linewidth of the pure Al nanoholes, shows a noticeable narrowed linewidth at 75°. We can distinctly observe ~8 nm narrow linewidth in Fig. 2(f) for the Al-Si heterostructures. To explain the mechanism of dissipation loss in the hybrid Si-Al metasurface, we performed the electromagnetic field distribution (EFD) using the commercial finite difference time domain (FDTD) software (see Appendix A.3). The simulation results demonstrate that the resonant mode characteristics of the heterostructures are similar to that of the plasmonic Al nanostructures [19,34]. The EFD in the x–y plane shows that the electromagnetic field is mainly located at the sidewall of the heterostructures. But we can observe a non-negligible electromagnetic field distribution inside the nanoholes due to introducing the low-loss Si nanoholes. The electromagnetic field decays exponentially in the y–z plane. The above results suggest that the narrowest linewidth can be achieved in the Al-Si heterostructures after introducing the low-loss nanostructures with high refraction.

Different from the plasmonic nanostructures, which can confine the light in the outside of the nanostructures, the dielectric nanostructures with high indices can concentrate light field into their inside. They manipulate optically induced Mie resonances. To clarify the mechanism of the heterostructures in narrowing the resonant linewidth, the resonant characteristics of the Si nanoholes are analyzed individually. For the scattered field of the Si nanohole arrays in the Cartesian coordinate system, the electric dipole and magnetic dipole can be written as follows [35,36]:

$$E_{\varphi}^{P}(r,\varphi,\theta) = \frac{k_d^2 e^{ik_d r}}{4\pi\varepsilon_0\varepsilon_d r}(p_y\cos\varphi - p_x\sin\varphi),$$
$$E_{\theta}^{P}(r,\varphi,\theta) = \frac{k_d^2 e^{ik_d r}}{4\pi\varepsilon_0\varepsilon_d r}(p_x\cos\varphi\cos\theta + p_y\sin\varphi\cos\theta - p_z\sin\theta), \quad (2)$$

$$E_{\varphi}^{m}(r,\varphi,\theta) = \sqrt{\frac{\mu_0}{\varepsilon_0\varepsilon_d}}\frac{k_d^2 e^{ik_d r}}{4\pi r}(-m_x\cos\varphi\cos\theta - m_y\sin\varphi\cos\theta + m_z\sin\varphi),$$
$$E_{\theta}^{m}(r,\varphi,\theta) = \sqrt{\frac{\mu_0}{\varepsilon_0\varepsilon_d}}\frac{k_d^2 e^{ik_d r}}{4\pi r}(m_y\cos\varphi - m_x\sin\varphi). \quad (3)$$

Here, $\boldsymbol{P} = (p_x, p_y, p_z)$ and $\boldsymbol{m} = (m_x, m_y, m_z)$ denote the electrical dipole and magnetic dipole, θ and φ the illuminating angle and the azimuthal angle of the spherical coordinate system, and k_d the wavelength vector of the dielectric nanosphere. The optical excitations of the Si nanostructures can be tuned by sizes and shapes that are derived from discrete electronic levels in the conduction and valence bands [24,35,37]. Notably, the optical characteristic of the Si nanohole arrays shows the angle dependence in Eqs. (2) and (3). The resonant modes of the Si nanoholes can be modulated by varying the θ and φ (see

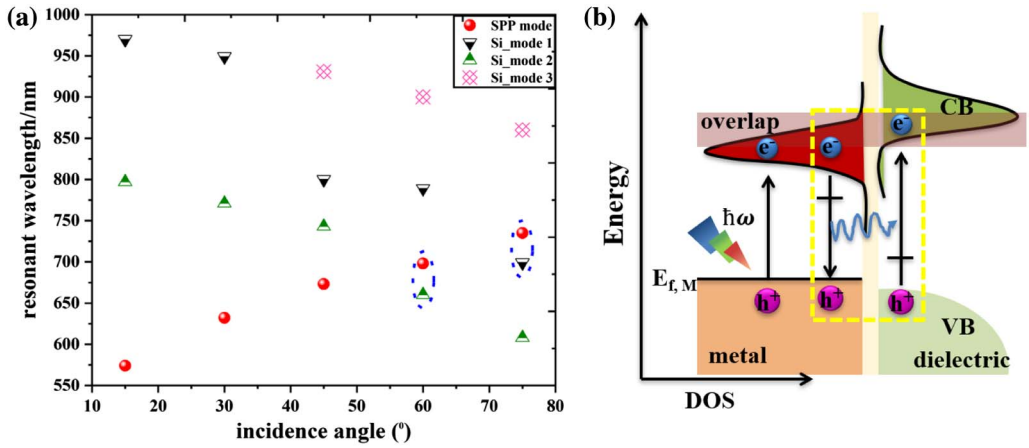

Fig. 3. Mechanism of Al-Si heterostructures. (a) The resonant modes of the Al nanostructures and the Si nanostructures under varied incidence angles. (b) The energy levels of the Al nanostructures and Si nanostructures. The resonant modes of the Si nanostructures will couple to the $(-1, 0)$ SPP mode in case of spectral overlapping.

Appendices A.4–A.6). Figure 3(a) demonstrates that the Si nanohole arrays exhibit three resonant modes labeled by Si_mode 1, Si_mode 2, and Si_mode 3, respectively. The Si_mode 1 and Si_mode 2 in the NIR region blue shift with increasing θ. A new resonant mode (Si_mode 3) will emerge when the incidence angle is larger than 45° and blue shifts. For pure Al nanostructures, the resonant modes of the Al nanostructures are angle-dependent [5,19], and they have red shifted when increasing the incident angle (see Appendices A.7 and A.8). By modulating θ, Si_mode 1 will couple to the $(-1, 0)$ SPP mode at 75° incidence. Si_mode 2 will couple to the $(-1, 0)$ SPP mode at 60° incidence [Fig. 3(a)]. As resonators, the Al nanostructures will couple to the excitons of the Si nanostructures through near-field interactions when their spectra overlap. The interaction results in narrowing the linewidth [Fig. 3(b)]. Therefore, optical excitations of Al-Si heterostructures can be realized through designing the resonant modes of metal and dielectric nanostructures.

The above results demonstrate a narrowing resonant linewidth of 8 nm by adopting the heterostructures. To further

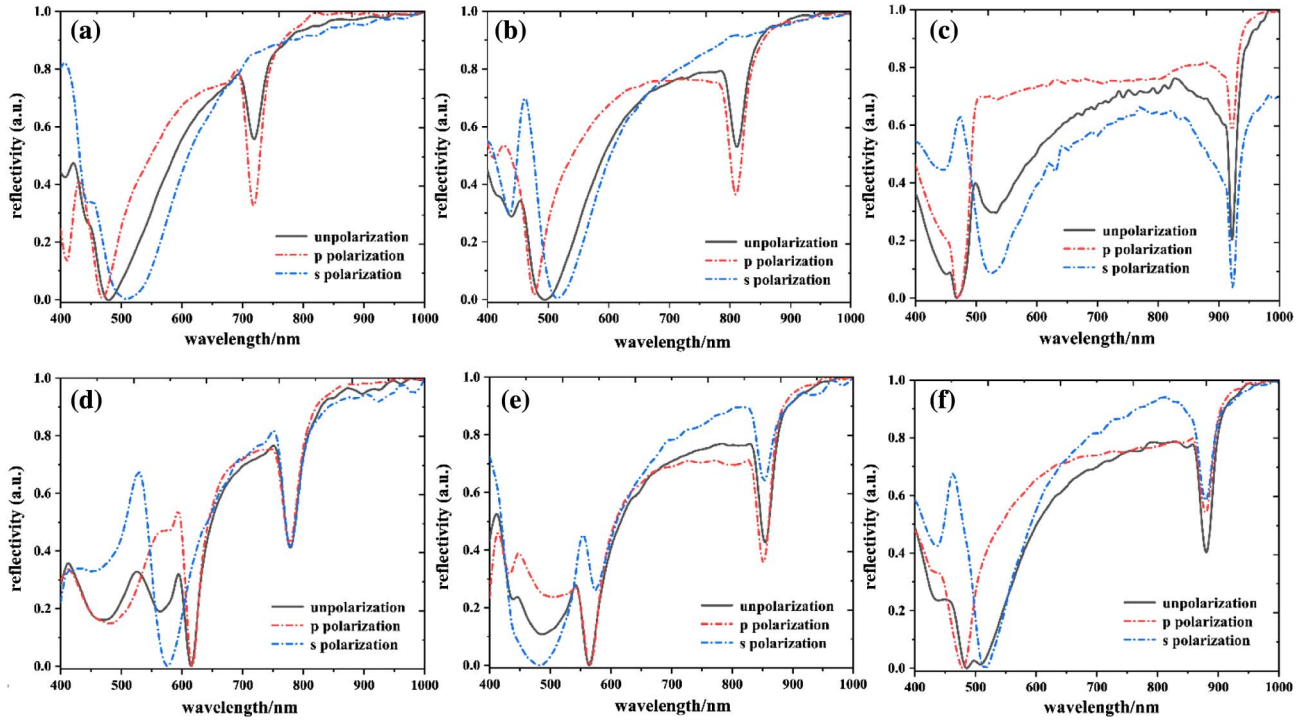

Fig. 4. Polarization-dependent optical properties of the heterostructures with an azimuthal angle of 0° by tuning the incident angles of (a) 30°, (b) 45°, and (c) 75° and with an illumination angle 60° by tuning the azimuthal angles of (d) 60°, (e) 75°, and (f) 90°.

investigate the optical properties of the heterostructures for dedicated applications, we recorded reflectance spectra of the heterostructures by changing φ and θ for polarization-dependent properties. Figures 4(a)–4(c) clearly show the reflectance spectra at characteristic θ with φ set as 0°. Figures 4(d)–4(f) demonstrate the polarization-dependent properties of reflectance spectra at characteristic φ with θ set as 60°. Because of the 4-fold symmetry of the tetragonal array of the heterostructures, similar results can be observed when φ equals 0°, 15°, and 30°. Figures 4(a)–4(c) clearly demonstrate that the $(-1, 0)$ SPP mode mainly depends on the p-polarization when θ is set as 30° and 45°, respectively. It is interesting to find that the unpolarized spectra of the $(-1, 0)$ SPP mode are the sum of p-polarization and s-polarization at θ being 75°. Figures 4(d)–4(f) intuitively exhibit that the reflectance spectra of the $(-1, 0)$ SPP mode are mainly the sum of p-polarization and s-polarization at φ of 60°, 75°, and 90°. The polarization-dependent property of the heterostructures can be used for the detection of the polarization of an unknown light source as well as other polarization-related applications [11].

3. CONCLUSION

In summary, we successfully fabricate metal/dielectric heterostructures consisting of the periodic metal arrays (Al) and dielectric nanostructures (Si). By introducing the low-loss Si nanostructures, the resonant band with a linewidth of ~8 nm can be narrowed by a factor of 66.7% in comparison with aluminum nanostructures. Moreover, the modulation range of the resonant wavelength based on the heterostructures can be engineered in a broader wavelength range from 600 to 900 nm, which is derived from the heterostructures critically depending on the illumination angle (θ) and the azimuthal angle (φ). We predict that the narrow linewidth based on the heterostructures can serve as a promising substrate for surface-enhanced spectroscopy and biosensors.

APPENDIX A: METHODS

A photoresist layer TU2-70 with 200 nm thickness was spin-coated on the silicon wafer (Obducat Technologies AB, Sweden). The nanopatterns were replicated from a nickel mold (hole array with 450-nm period and 250-nm hole diameter) to photoresist utilizing the Eitre-6 nanoimprint lithography system (Obducat Technologies AB, Sweden). A thermal nanoimprint on the nickel mold was taken with the intermediate polymer sheet (IPS, Obducat Technologies AB, Sweden) at 150°C with 40 bar (1 bar = 10^5 Pa) pressure for 3 min. Upon the removal from the hard mold, the nanopattern can be formed on the IPS surface and act as the soft mold during the UV-nanoimprint process. The replica IPS soft mold was placed on the TU2-170 photoresist surface and was imprinted at 65°C under 30 bar pressure for 5 min as well as UV-exposed for 1 min. To isolate the photoresist nanopatterns after the separation of the IPS from the resist, we precisely removed the residual layer on the bottom via the Q150 micro-wave plasma etching system (Alpha, Germany) with a gas mixture of O_2 (100 sccm; sccm, standard cubic centimeters per minute) and Ar (100 sccm) plasma at a chamber pressure of 60 Pa and a power density of 300 W for 60 s, resulting in the change of the hole array (450-nm period, 300-nm hole in diameter, about 2-nm-thick residual photoresist layer). Silicon nanoholes of 100-nm depth were formed via the inductively coupled plasma (ICP) etching system with photoresist nanoholes as mask. The heterostructures will be formed by spin-coating an approximately 80-nm Al film by TEMD-500 thermal evaporation. The large-scale and high-quality heterostructures with 450-nm period and 240-nm diameter have been formed.

1. Imaginary Part of the Refractive Index of Material Si

According to the data from Ref. [38], we plot the extinction coefficient of material Si in the Fig. 5. The extinction coefficient of material Si is near zero in the visible and the NIR spectral ranges. Si is a superior candidate in low-loss materials.

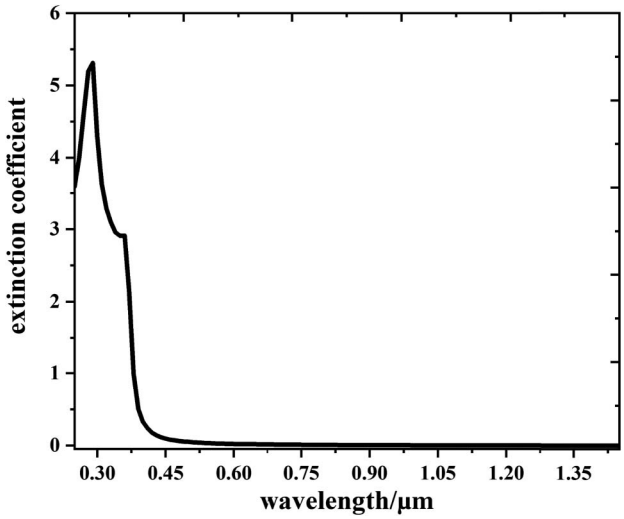

Fig. 5. Imaginary part of the refractive index of the Si material is near zero in the visible and NIR regions.

2. Measurement of Angle-Resolved Reflectance Spectra

The angle-resolved reflectivity spectra were measured for the pure Al, pure Si, and Al-Si heterostructures nanoholes on silicon wafer by utilizing a home-built UV-visible-NIR spectrometer. The schematic of the angle-resolved reflectivity spectrometer is illustrated in Fig. 6(a). The device is composed of light source (AvaLight-DH-S-BAL), spectrometer (vaSpec-NIR256/512-1), and sample platform (including angle-resolved mould). The angles of θ and φ are defined as illumination angle and azimuthal angle in the Fig. 6(b), respectively. The angles of θ and φ can be modulated through changing the position of optical fiber in the angle-resolved mould and rotating the sample in x–y plane.

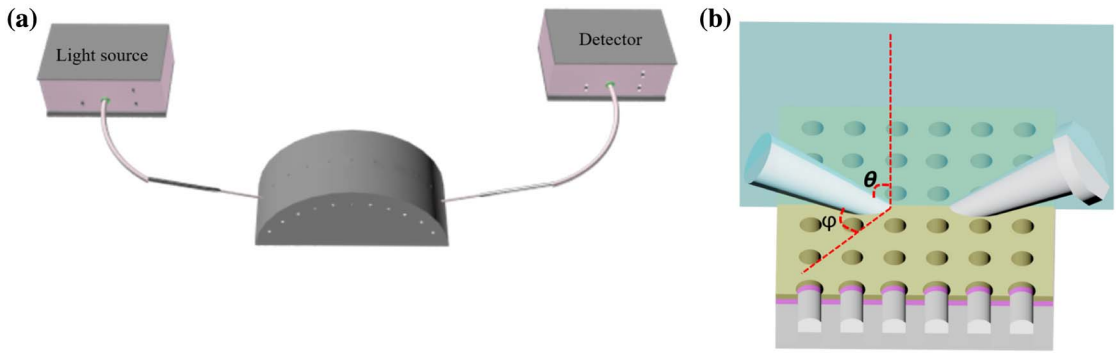

Fig. 6. (a) The spectral analysis equipment of the angle-resolved spectrometer. (b) The diagram of θ and φ, defining the illumination angle and the azimuthal angle, respectively.

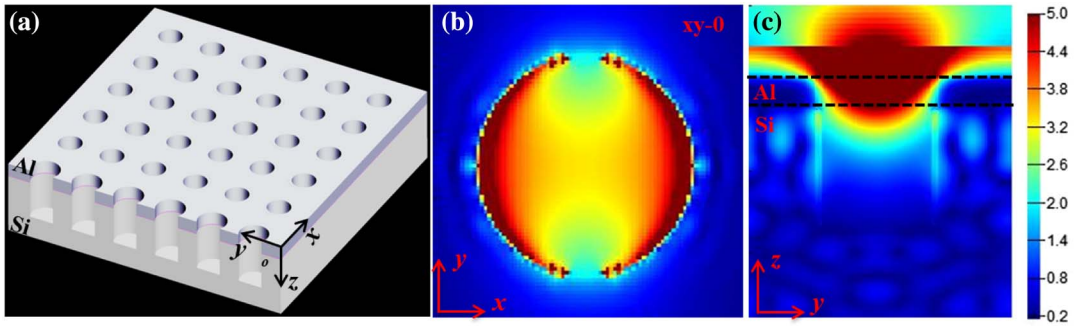

Fig. 7. Electromagnetic field distribution using commercial FDTD software. (a) The schematic illustration of heterostructures. (b) The electromagnetic field distribution in the x–y plane. (c) The electromagnetic field distribution in the y–z plane.

3. *E*-field Distribution of Heterostructures

Figure 7 shows the electromagnetic field (*E*-field) distribution using commercial FDTD software. The illustration of heterostructures is displayed in the Fig. 7(a). The *E*-field distribution in the x–y plane shows that the *E*-field is mainly located at the sidewall of heterostructures [Fig. 7(b)]. But, we can observe non-negligible *E*-field distribution inside the nanoholes due to introducing the low-loss Si nanoholes. The electromagnetic field decays exponentially in the y–z plane [Fig. 7(c)].

4. SEM Image of Si Nanoholes

The morphology of Si metasurfaces is measured by utilizing scanning electron microscopy (SEM). Figure 8 demonstrates that large-area and high-quality Si metasurfaces can be fabricated by NIL technique. The periods P_x and P_y are both 450 nm and the width of nanoholes is 240 nm.

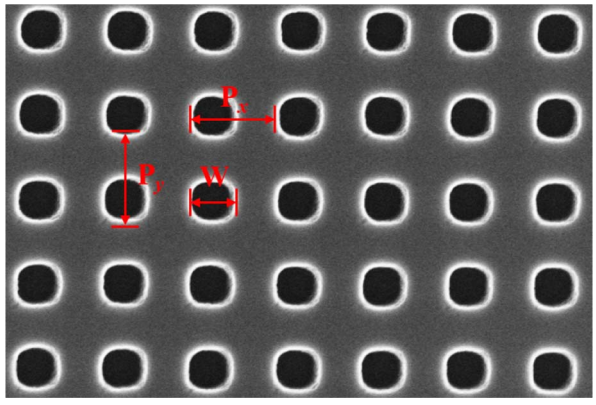

Fig. 8. Top-view SEM image of the Si nanoholes, where P_x equal to P_y denotes the 450 nm period and W the 240 nm width of the nanoholes.

5. Reflectance Spectra of Si Nanoholes Arrays under Varied Illumination Angles

The dielectric nanostructures with high refractive index are favorable to enhance light-matter interaction in nanoscale, benefiting from the advantages of low loss, optical magnetism, and multipolar responses. The materials, such as Si, Ge, TiO_2, are commonly used as dielectric metastructures due to the characteristic of high index and low loss in the visible range. The optical excitations of Si nanostructures can be tuned by size and shapes that are derived from discrete electronic levels in conductions and valence bands. Like plasmonic nanoarrays, Si nanoholes arrays have different colors that can be observed by the naked eye when tilted toward different angles. Therefore, we quantitatively characterized angle-resolved reflectance

spectra of Si nanoholes arrays by changing the illumination angle (θ) and the azimuthal angle (φ) of the samples. First, the reflectance spectra in case of changing θ from 15° to 60° are recorded and the results have been listed in Fig. 9. When θ is smaller than 30°, there are two resonant peaks in the reflectance spectra. Once θ is larger than 30°, the third resonant mode will occur in the reflectance spectra. We can distinctly observe that all the resonant modes will blue shift as θ increases. Next, a series of azimuthal angle-resolved optical measurements was performed to study the resonant modes of Si nanoholes arrays. The results shown in Fig. 9 demonstrate that the resonant modes located at the larger wavelength will slightly shift.

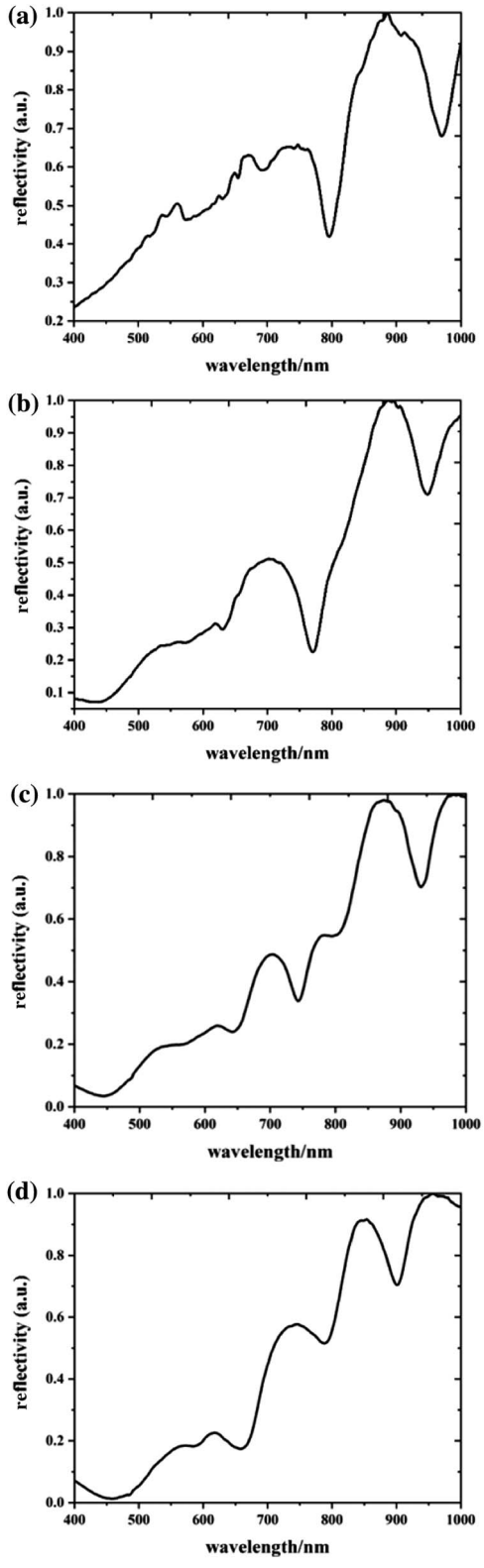

Fig. 9. Reflectance spectra of the Si nanoholes arrays under varied θ. The resonant modes are at (a) 15°, (b) 30°, (c) 45°, and (d) 60°.

6. Reflectance Spectra of Si Nanoholes Arrays under Varied Azimuthal Angles

The optical dependence of Si nanoholes on azimuthal angles (φ) has been investigated. Figure 10 demonstrates that the resonant modes of Si nanoholes will blue shift with increasing φ.

7. SEM Image of Al Nanoholes

The morphology of Al metasurfaces is measured by utilizing scanning electron microscopy (SEM). Figure 11 demonstrates

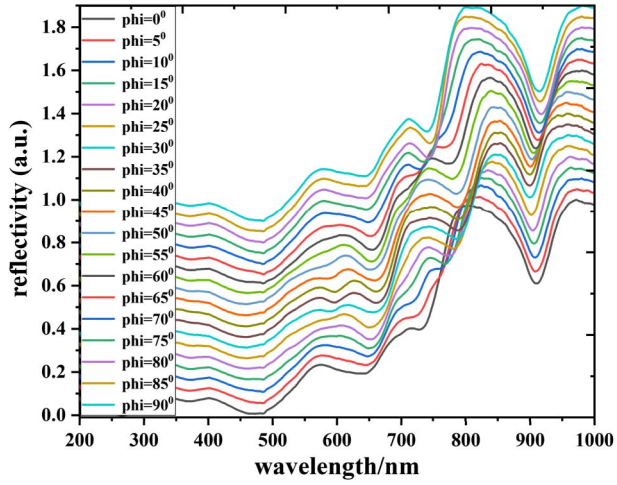

Fig. 10. Reflectance spectra of the Si nanoholes arrays under varied φ when θ is equal to 60°. The φ changes from 0° to 90°, and the step is 5°.

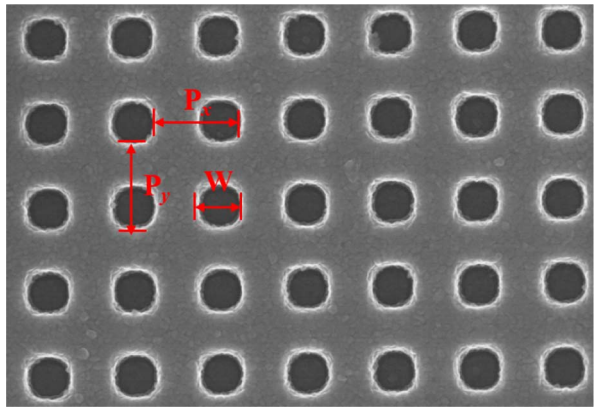

Fig. 11. Top-view SEM image of Al nanoholes, where P_x equal to P_y denotes the 450 nm period and W the 240 nm width of the nanoholes.

that large-area and high-quality Al metasurfaces can be obtained by NIL technique. The periods P_x and P_y are both 450 nm and the width of nanoholes is 240 nm.

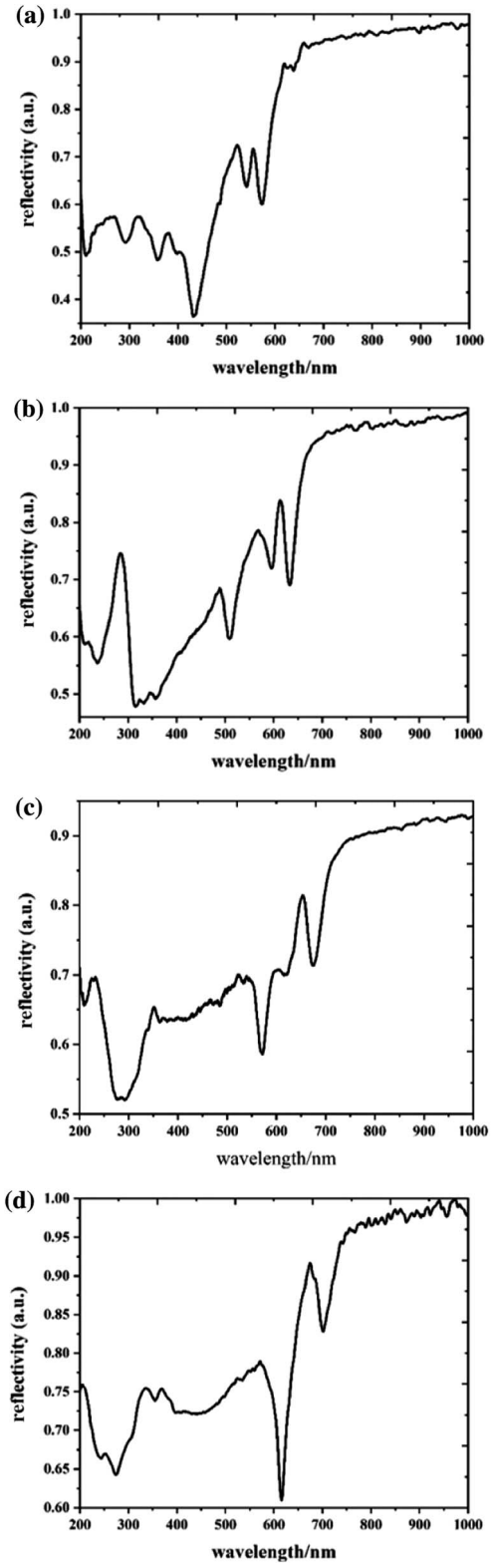

Fig. 12. Reflection spectra under different incident angles are collected by the angle-resolved spectrometer when the azimuthal angle equals 0°. The illuminating angle equals (a) 15°, (b) 30°, (c) 45°, and (d) 60°.

8. Optical Properties of Al Nanoholes Arrays

The well-defined Al plasmonic nanoholes are quantitatively characterized by utilizing the home-built angle-resolved UV-visible-NIR spectrometer. The reflectance spectra in case of varied illumination angles are recorded, and the results have been shown in Fig. 12. Seriously, there are two resonance peaks displayed in those reflectance spectra. The mode in the larger wavelength obviously shows the trend of red shift and can be attributed to the (−1, 0) SPP modes. Likewise, the mode at the shorter wavelength red shifts. These modes obtained in the experiment can be explained by the classical dispersion of an ideal grating:

$$\frac{2\pi}{\lambda_{\mathrm{SPP}}}\sqrt{\frac{\varepsilon_{\mathrm{Al}}\cdot\varepsilon}{\varepsilon_{\mathrm{Al}}+\varepsilon}} = \sqrt{\left(\frac{2\pi}{\lambda_{\mathrm{SPP}}}\sin\theta\sin\varphi+m\frac{2\pi}{P}\right)^2+\left(\frac{2\pi}{\lambda_{\mathrm{SPP}}}\sin\theta\cos\varphi+n\frac{2\pi}{P}\right)^2}.$$

Funding. National Natural Science Foundation of China (12104329, 12174324, 92161118); Ministry of Science and Technology of the People's Republic of China (2021YFA1201502).

Acknowledgment. The authors thank Professor Lihua Qian for polishing the essay's language and Dr. Jingyu Wang and Dr. Peiwen Ren for helpful discussions.

Disclosures. The authors declare no conflicts of interest.

Data Availability. Data underlying the results presented in this paper are not publicly available at this time but may be obtained from the authors upon reasonable request.

REFERENCES

1. L. Wen, L. Liang, X. Yang, Z. Liu, B. Li, and Q. Chen, "Multiband and ultrahigh figure-of-merit nanoplasmonic sensing with direct electrical readout in Au-Si nanojunctions," ACS Nano **13**, 6963–6972 (2019).
2. U. Aslam, V. G. Rao, S. Chavez, and S. Linic, "Catalytic conversion of solar to chemical energy on plasmonic metal nanostructures," Nat. Catal. **1**, 656–665 (2018).
3. C. Ji, K.-T. Lee, T. Xu, J. Zhou, H. J. Park, and L. J. Guo, "Engineering light at the nanoscale: structural color filters and broadband perfect absorbers," Adv. Opt. Mater. **5**, 1700368 (2017).
4. M. Gao, W. Yang, Z. Wang, S. Lin, J. Zhu, and Z. Yang, "Plasmonic resonance-linewidth shrinkage to boost biosensing," Photon. Res. **8**, 1226–1235 (2020).
5. A. K. Yang, A. J. Hryn, M. R. Bourgeois, W.-K. Lee, J. Hu, G. C. Schatz, and T. W. Odom, "Programmable and reversible plasmon mode engineering," Proc. Natl. Acad. Sci. USA **113**, 14201–14206 (2016).
6. V. G. Kravets, A. V. Kabashin, W. L. Barnes, and A. N. Grigorenko, "Plasmonic surface lattice resonances: a review of properties and applications," Chem. Rev. **118**, 5912–5951 (2018).
7. Y. Chu, E. Schonbrun, T. Yang, and K. B. Crozier, "Experimental observation of narrow surface plasmon resonances in gold nanoparticle arrays," Appl. Phys. Lett. **93**, 181108 (2008).
8. B. Liu, S. Chen, J. Zhang, X. Yao, J. Zhong, H. Lin, T. Huang, Z. Yang, J. Zhu, S. Liu, C. Lienau, L. Wang, and B. Ren, "A plasmonic sensor array with ultrahigh figures of merit and resonance linewidths down to 3 nm," Adv. Mater. **30**, 1706031 (2018).

9. X. Zhu, Y. Zhang, J. Zhang, J. Xu, Y. Ma, Z. Li, and D. Yu, "Ultrafine and smooth full metal nanostructures for plasmonics," Adv. Mater. **22**, 4345–4349 (2010).
10. S. Zhang, G.-C. Li, Y. Chen, X. Zhu, S.-D. Liu, D. Lei, and H. Duan, "Pronounced Fano resonance in single gold split nanodisks with 15 nm split gaps for intensive second harmonic generation," ACS Nano **10**, 11105–11114 (2016).
11. M. P. Knudson, R. Li, D. Wang, W. Wang, R. D. Schaller, and T. W. Odom, "Polarization-dependent lasing behavior from low-symmetry nanocavity arrays," ACS Nano **13**, 7435–7441 (2019).
12. M. L. Tseng, J. Yang, M. Semmlinger, C. Zhang, P. Nordlander, and N. J. Halas, "Two-dimensional active tuning of an aluminum plasmonic array for full-spectrum response," Nano Lett. **17**, 6034–6039 (2017).
13. K. V. Sreekanth, Y. Alapan, M. ElKabbash, E. Ilker, M. Hinczewski, U. A. Gurkan, A. D. Luca, and G. Strangi, "Extreme sensitivity biosensing platform based on hyperbolic metamaterials," Nat. Mater. **15**, 621–627 (2016).
14. Y. Liang, K. Koshelev, F. Zhang, H. Lin, S. Lin, J. Wu, B. Jia, and Y. Kivshar, "Bound states in the continuum in anisotropic plasmonic metasurfaces," Nano Lett. **20**, 6351–6356 (2020).
15. Y. Liang, H. Lin, S. Lin, J. Wu, W. Li, F. Meng, Y. Yang, X. Huang, B. Jia, and Y. Kivshar, "Hybrid anisotropic plasmonic metasurfaces with multiple resonances of focused light beams," Nano Lett. **21**, 8917–8923 (2021).
16. S. I. Azzam, V. M. Shalaev, A. Boltasseva, and A. V. Kildishev, "Formation of bound states in the continuum in hybrid plasmonic-photonic systems," Phys. Rev. Lett. **121**, 253901 (2018).
17. M. S. Bin-Alam, O. Reshef, Y. Mamchur, M. Z. Alam, G. Carlow, J. Upham, B. T. Sullivan, J.-M. Ménard, M. J. Huttunen, R. W. Boyd, and K. Dolgaleva, "Ultra-high-*Q* resonances in plasmonic metasurfaces," Nat. Commun. **12**, 974 (2021).
18. N. J. J. van Hoof, D. R. Abujetas, S. E. T. ter Huurne, F. Verdelli, G. C. A. Timmermans, J. A. Sánchez-Gil, and J. G. Rivas, "Unveiling the symmetry protection of bound states in the continuum with terahertz near-field imaging," ACS Photon. **8**, 3010–3016 (2021).
19. J. Zheng, W. Yang, J. Wang, J. Zhu, L. Qian, and Z. Yang, "An ultra-narrow SPR linewidth in the UV region for plasmonic sensing," Nanoscale **11**, 4061–4066 (2019).
20. J. B. Khurgin and A. Boltasseva, "Reflecting upon the losses in plasmonics and metamaterials," MRS Bull. **37**, 768–779 (2012).
21. A. I. Kuznetsov, A. E. Miroshnichenko, M. L. Brongersma, Y. S. Kivshar, and B. Luk'yanchuk, "Optically resonant dielectric nanostructures," Science **354**, aag2472 (2016).
22. K. Koshelev and Y. Kivshar, "Dielectric resonant metaphotonics," ACS Photon. **8**, 102–112 (2021).
23. Y. Yang, O. D. Miller, T. Christensen, J. D. Joannopoulos, and M. Soljačić, "Low-loss plasmonic dielectric nanoresonators," Nano Lett. **17**, 3238–3245 (2017).
24. C. Wei and Y. S. Zhao, "Photonic applications of metal–dielectric heterostructured nanomaterials," ACS Appl. Mater. Interfaces **8**, 3703–3713 (2016).
25. M. Achermann, "Exciton–plasmon interactions in metal–semiconductor nanostructures," J. Phys. Chem. Lett. **1**, 2837–2843 (2010).
26. Y. Q. Qu and X. F. Duan, "Progress, challenge and perspective of heterogeneous photocatalysts," Chem. Soc. Rev. **42**, 2568–2580 (2013).
27. R. Jiang, B. Li, C. Fang, and J. Wang, "Metal/semiconductor hybrid nanostructures for plasmon enhanced applications," Adv. Mater. **26**, 5274–5309 (2014).
28. S. K. Dutta, S. K. Mehetor, and N. Pradhan, "Metal semiconductor heterostructures for photocatalytic conversion of light energy," J. Phys. Chem. Lett. **6**, 936–944 (2015).
29. C. Jia, X. Li, N. Xin, Y. Gong, J. Guan, L. Meng, S. Meng, and X. Guo, "Interface-engineered plasmonics in metal/semiconductor heterostructures," Adv. Energy Mater. **6**, 1600431 (2016).
30. X.-C. Ma, Y. Dai, L. Yu, and B.-B. Huang, "Energy transfer in plasmonic photocatalytic composites," Light Sci. Appl. **5**, e16017 (2016).
31. A. I. Barreda, M. Zapata-Herrera, I. M. Palstra, L. Mercadé, J. Aizpurua, A. F. Koenderink, and A. Martínez, "Hybrid photonic-plasmonic cavities based on the nanoparticle-on-a-mirror configuration," Photon. Res. **9**, 2398–2419 (2021).
32. X. X. Han, W. Ji, B. Zhao, and Y. Ozaki, "Semiconductor-enhanced Raman scattering: active nanomaterials and applications," Nanoscale **9**, 4847–4861 (2017).
33. M. Gao, Y. He, Y. Chen, T.-M. Shih, W. Yang, J. Wang, F. Zhao, M.-D. Li, H. Chen, and Z. Yang, "Tunable surface plasmon polaritons and ultrafast dynamics in 2D nanohole arrays," Nanoscale **11**, 16428–16436 (2019).
34. K. Yang, J. Wang, X. Yao, D. Lyu, J. Zhu, Z. Yang, B. Liu, and B. Ren, "Large-area plasmonic metamaterial with thickness-dependent absorption," Adv. Opt. Mater. **9**, 2001375 (2021).
35. T. Liu, R. Xu, P. Yu, Z. Wang, and J. Takahara, "Multipole and multimode engineering in Mie resonance-based metastructures," Nanophotonics **9**, 1115–1137 (2020).
36. A. B. Evlyukhin, C. Reinhardt, and B. N. Chichkov, "Multipole light scattering by nonspherical nanoparticles in the discrete dipole approximation," Phys. Rev. B **84**, 235429 (2011).
37. E. Cao, W. Lin, M. Sun, W. Liang, and Y. Song, "Exciton-plasmon coupling interactions: from principle to applications," Nanophotonics **7**, 145–167 (2018).
38. C. Schinke, P. C. Peest, J. Schmidt, R. Brendel, K. Bothe, M. R. Vogt, I. Kröger, S. Winter, A. Schirmacher, S. Lim, H. T. Nguyen, and D. MacDonald, "Uncertainty analysis for the coefficient of band-to-band absorption of crystalline silicon," AIP Adv. **5**, 067168 (2015).